

# Sustainable wood electronics by iron-catalyzed laser-induced graphitization for large-scale applications

Christopher H. Dreimol <sup>1,2</sup>, Huizhang Guo<sup>1</sup>, Maximilian Ritter <sup>1,2</sup>, Tobias Keplinger<sup>1</sup>, Yong Ding <sup>1,2</sup>, Roman Günther<sup>3,4</sup>, Erik Poloni <sup>5,6</sup>, Ingo Burgert <sup>1,2</sup>✉ & Guido Panzarasa <sup>1</sup>✉

Ecologically friendly wood electronics will help alleviating the shortcomings of state-of-art cellulose-based “green electronics”. Here we introduce iron-catalyzed laser-induced graphitization (IC-LIG) as an innovative approach for engraving large-scale electrically conductive structures on wood with very high quality and efficiency, overcoming the limitations of conventional LIG including high ablation, thermal damages, need for multiple lasing steps, use of fire retardants and inert atmospheres. An aqueous bio-based coating, inspired by historical iron-gall ink, protects wood from laser ablation and thermal damage while promoting efficient graphitization and smoothening substrate irregularities. Large-scale (100 cm<sup>2</sup>), highly conductive ( $\geq 2500 \text{ S m}^{-1}$ ) and homogeneous surface areas are engraved single-step in ambient atmosphere with a conventional CO<sub>2</sub> laser, even on very thin ( $\sim 450 \mu\text{m}$ ) wood veneers. We demonstrate the validity of our approach by turning wood into highly durable strain sensors, flexible electrodes, capacitive touch panels and an electroluminescent LIG-based device.

<sup>1</sup>Wood Materials Science, Institute for Building Materials, ETH Zürich, 8093 Zürich, Switzerland. <sup>2</sup>Cellulose & Wood Materials Laboratory, Empa, 8600 Dübendorf, Switzerland. <sup>3</sup>Laboratory of Adhesives and Polymer Materials, Institute of Materials and Process Engineering, ZHAW Zürich University of Applied Sciences, 8401 Winterthur, Switzerland. <sup>4</sup>Multifunctional Materials, Department of Materials, ETH Zürich, 8093 Zürich, Switzerland. <sup>5</sup>Complex Materials, Department of Materials, ETH Zürich, 8093 Zürich, Switzerland. <sup>6</sup>Present address: High Enthalpy Flow Diagnostics Group, Institute of Space Systems, University of Stuttgart, 70569 Stuttgart, Germany. ✉email: [iburgert@ethz.ch](mailto:iburgert@ethz.ch); [guido.panzarasa@ifb.baug.ethz.ch](mailto:guido.panzarasa@ifb.baug.ethz.ch)

Developing electronic devices from renewable and biodegradable materials using environmentally friendly manufacturing routes (“green electronics”) is mandatory to meet the demands of a sustainable society<sup>1</sup>. The foreseen implementation of the Internet-of-Things (IoT) approach to smart buildings and even cities poses unmet challenges in terms of scale and durability of sustainable electronic materials<sup>2,3</sup>. State-of-art green electronics is nowadays dominated by relatively small, disposable devices made from (nano-)cellulose-based materials<sup>4–6</sup>. However, their sustainability may be challenged by the many demanding steps, in terms of amount of energy and chemicals, needed for the isolation and reassembly of cellulose into functional materials. Using wood as substrate for electronic devices can help solving this problem at the root. Wood materials are also especially useful for applications requiring not only high mechanical strength and scalability, such as structural health monitoring (e.g., strain sensors incorporated in load-bearing structures), but also valuable esthetics and haptics (such as touch-screens and light displays as human-machine interfaces in smart buildings).

Wood is a renewable and biodegradable CO<sub>2</sub>-storing natural resource, an excellent state-of-art building material with highly appreciated esthetics and haptics, lightweight but with high mechanical strength. The development of wood electronics has so far been limited by the complex wood structure and the lack of intrinsic electrical conductivity. Previous attempts toward electrically conductive wood materials have included the surface coating with metal nanowires<sup>7</sup> and carbon-based inks<sup>8</sup>, as well as bulk impregnation e.g. with low-melting metals<sup>9</sup>. In these approaches, irrespective of their limited sustainability, wood has been used as a passive substrate. As for other biological substrates, graphitizing wood under proper conditions can result in graphene- and graphite-like materials with reasonable electrical properties (>500 S m<sup>-1</sup> and <1 kΩ □<sup>-1</sup>)<sup>10–13</sup>. However, this usually happens at the expense of structural and mechanical integrity. Finding a way to confine graphitization selectively at the wood surface, down to several microns but leaving the bulk intact, would open up new avenues for wood electronics.

Laser-induced graphitization (LIG) has been used to convert a variety of inorganic<sup>14,15</sup> and organic precursors into electrically conductive materials<sup>16–18</sup>. This graphitization process can be best described as a combined photothermal and photochemical conversion of a precursor that leads to a porous carbonaceous material. LIG is a cost-effective technique featuring high processing speeds and flexibility, making possible to combine laser-engraving of graphitized patterns with controlled morphology<sup>19</sup> together with laser-cutting. First attempts of biological materials laser-induced graphitization<sup>16,20</sup> led to products with reasonable, yet not entirely sufficient, electric and structural properties for most envisaged applications, such as large-scale sensors and actuators.

Wood is a challenging material for laser-induced graphitization. Due to the low thermal conductivity of wood (~0.2 W m<sup>-1</sup> K<sup>-1</sup>)<sup>21</sup>, its surface can undergo significant thermal degradation well before the bulk could reach the decomposition temperature, resulting in asymmetric shrinkage and mechanical stresses that result into cracks<sup>10</sup>. This problem is frequently encountered when highly localized heat sources are applied, as in laser-induced graphitization. Nevertheless, high temperatures (1200–3000 °C) are required to convert wood into graphite-like materials with reasonable electrical properties<sup>13,20</sup>. To reduce thermal damage and ablation rates, the lasing can be performed under an oxygen-free atmosphere (Ar or H<sub>2</sub>)<sup>16</sup>. Alternatively, the wood surface can be graphitized to a dense char layer as a barrier against heat and mass transport, which is subsequently made electrically conductive via LIG<sup>17</sup>. So far, this two-step approach for LIG in ambient

atmosphere has only been reported for wood and cellulose-based materials (paper and fabrics) impregnated with a fire-retardant (boric acid). Although slow engraving speeds, reduced power values, and multiple (up to five) lasing steps were employed, the resulting LIG structures were still inhomogeneous and showed numerous cracks<sup>17</sup>. Photo-assisted graphitization of native wood by means of femtosecond laser systems was suggested to minimize thermal damage, but satisfactory electrical conductivity could only be achieved with low engraving speeds (from 5 to 15 mm s<sup>-1</sup>) resulting in disproportionate process times. Even under these conditions, substrate ablation could only be reduced to around 300–500 μm<sup>20</sup>, causing excessive damage to thin (500–1500 μm) decorative wood veneers.

Here we demonstrate an innovative and convenient method for engraving highly conductive (≥20 Ω □<sup>-1</sup> and up to 2500 S m<sup>-1</sup>) LIG patterns on the surface of thin wood veneers, with a single lasing step under ambient atmosphere, using a conventional CO<sub>2</sub> laser source and high writing speeds. This approach, iron-catalyzed laser-induced graphitization (IC-LIG), takes advantage of the intumescent and thermo-catalytic properties of an iron-tannic acid ink of our formulation (Fig. 1a). Thanks to our approach, electrically conductive graphite-like structures can be engraved even on thin wood veneers (~0.4–1.5 mm) and paper substrates without ablation and thermal damage. This allows the fabrication of a variety of devices directly on wood, including the first reported example of an electroluminescent device made with a LIG electrode (Fig. 1b). Compared to recent LIG reports, we achieved conductivity values of up to 2500 S m<sup>-1</sup> on different wood substrates, an order of magnitude higher than the highest literature value (400 S m<sup>-1</sup>)<sup>20</sup>, with increased engraving speed (up to 35 times faster) and reduced energy consumption thanks to lasing only a single time with moderate laser power (Fig. 1c, Supplementary Table 1). These features make IC-LIG a highly efficient laser-induced graphitization method. We analyzed in detail the relevant electrical, morphological and compositional characteristics of the resulting LIG structures using state-of-art techniques, including 4-point probe measurements, Raman spectroscopy, optical and electron microscopy, and wide-angle X-ray diffraction. Furthermore, we demonstrated for the first time the homogeneity of the electrical properties of the obtained LIG-wood, mapping it over a very large area (100 cm<sup>2</sup>) using an innovative eddy-current measurement technique. To showcase the usefulness of IC-LIG for sustainable large-scale wood electronics, we developed four proof-of-concept applications, namely: a highly durable strain sensor suitable for structural health monitoring, a flexible electrode for motion tracking, a human-machine interface (capacitive touch panel) with the esthetics and haptics of wood, and the first example of an electroluminescent device made using LIG as electrode material.

## Results

Complexes of iron cations and polyphenols (such as tannic acid) have received increasing attention over the last decade thanks to their sustainability, biocompatibility and rich chemistry, making them of interest for a variety of applications ranging from functional coatings to the assembly of nanostructures<sup>22,23</sup>. Many of these researches, including the present one, have been inspired by the iron-gall ink used in Europe for writing manuscripts since the Middle Ages<sup>24,25</sup>. We chose tannic acid (TA) as a readily available natural polyphenol with well-known iron-complexing ability<sup>26</sup> and intumescent thermal behavior<sup>27</sup>. Mixing iron(III) citrate with excess tannic acid results in the instantaneous formation of insoluble complexes with a characteristic deep bluish-purple color (Supplementary Fig. 1)<sup>28</sup>. Compared to more common chloride, sulfate or nitrate salts, the use of iron(III) citrate

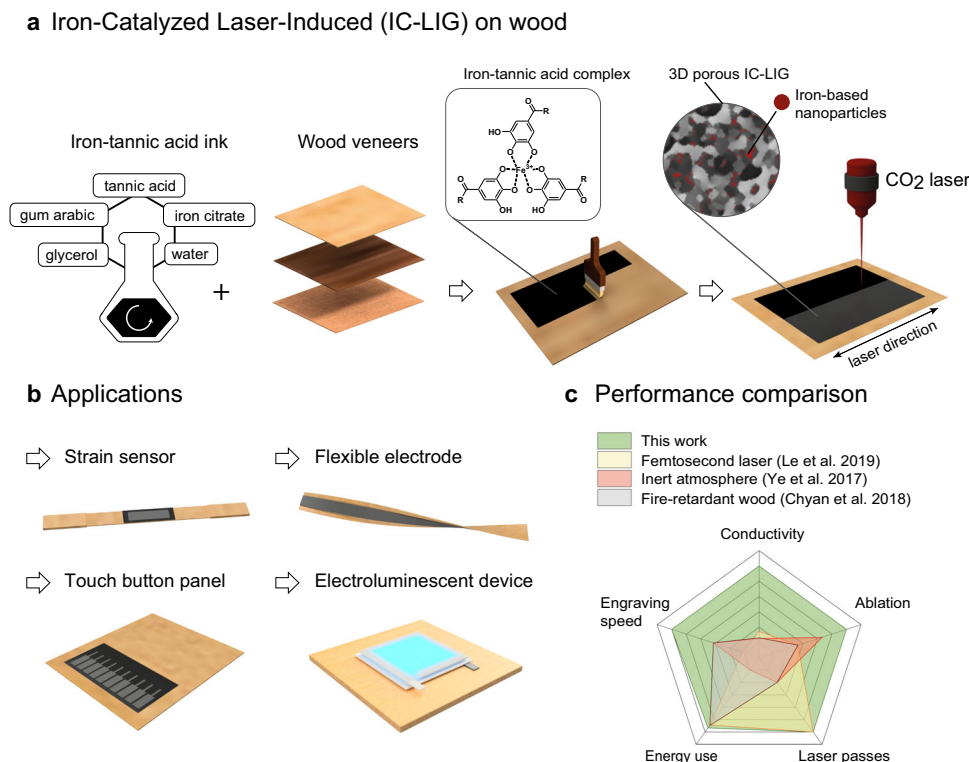


**Fig. 1** Iron-catalyzed laser-induced graphitization (IC-LIG) of wood and applications thereof. **a** Schematic representation of the IC-LIG process. The substrate (e.g., a wood veneer) is coated with an iron-tannic acid ink (the inset shows a simplified structure of the iron-tannic acid complex contained in the ink, see also Supplementary Fig. 1). The ink-coated wood veneer is then treated with a CO<sub>2</sub> laser to achieve IC-LIG (the inset shows a schematic of the resulting 3D porous iron-carbon composite). **b** Proof-of-concept applications demonstrated in this work for IC-LIG structures on wood veneers: a strain sensor, a flexible electrode, a touch buttons panel, and an electroluminescent device. **c** A radar plot comparing the performance of our IC-LIG with other previously published LIG approaches in terms of process parameters (faster engraving speed, lower energy use, only one laser pass needed) and quality (higher electrical conductivity, lower substrate ablation) of the resulting LIG materials (see also Supplementary Table 1).

helps to avoid the generation of hazardous gases during lasing and the uncontrolled introduction of heteroatomic dopants. Further addition of gum arabic facilitates to stabilize the complex in suspension<sup>29</sup>, resulting in a stable ink, while glycerol reduces crack formation upon drying.

The visual appearance of different native and ink-coated wood and paper substrates before and after a single laser passage is compared in Supplementary Fig. 2. All the uncoated substrates were severely damaged (some were completely incinerated, like balsa wood and the cellulose paper we used as control), while for the ink-coated ones the laser treatment resulted in a homogeneous carbonaceous layer with no visible cracks. The ink was deposited on all samples with a paintbrush. On wood veneers, it was found to penetrate on average only into the first cell layers ( $\leq 50 \mu\text{m}$ ), forming a layer of variable thickness (between 20 and 80  $\mu\text{m}$  depending on the wood species and surface roughness, Supplementary Fig. 3a, b) which smoothed the otherwise naturally irregular wood surface. By contrast, paper was almost completely impregnated.

We laser-treated large ( $\sim 100 \text{ cm}^2$ ) samples (Fig. 2a, b), then measured their sheet resistivity values using both a conventional four-point probe setup (Supplementary Fig. 3c) and a contactless, non-destructive eddy-current method (Fig. 2b and Supplementary Figs. 4 and 5). The values obtained with both techniques were in excellent agreement and confirmed the successful production of highly conductive materials for every tested wood species as well as for paper (Supplementary Fig. 3c). Despite the intrinsic structural anisotropy of wood substrates, no significant differences in sheet resistivity could be detected by performing the measurements in the direction parallel or perpendicular to the

lasing direction as well as to the wood fiber direction (Supplementary Fig. 3c), suggesting that neither the wood substrate nor the lasing direction could negatively affect the outcome of our process. The high uniformity of laser-treated areas was further demonstrated by the two-dimensional sheet resistivity maps obtained with eddy-current measurements (Fig. 2c, d and Supplementary Fig. 4). We point out that this is the first time that the homogeneity of such a large-area ( $100 \text{ cm}^2$ ) LIG surface is shown by a direct measurement.

A thorough analysis of characteristic Raman peaks<sup>16,30–32</sup> confirmed the presence of graphite-like materials in the laser-treated areas. Graphite-like carbon generally shows three distinct peaks in its Raman spectrum, the D-peak ( $\sim 1350 \text{ cm}^{-1}$ , associated with the breathing mode of  $sp^2$  atoms), the G-peak ( $\sim 1580 \text{ cm}^{-1}$ , due to the bond stretching of  $sp^2$  atoms pairs), and the 2D-peak ( $\sim 2970 \text{ cm}^{-1}$ , an overtone of the D band)<sup>30,33,34</sup>. To prove the successful graphitization of ink-coated samples, we mapped the G-peak band ( $1570\text{--}1580 \text{ cm}^{-1}$ , Fig. 2e) since the G-peak is always observed for graphitic materials ( $sp^2$  carbon systems). The dark red areas in the map are due to high-intensity G-peak bands, as can be seen from the corresponding region of interest (ROI,  $\sim 15 \times 15 \mu\text{m}^2$ ) in Fig. 2f (ROI-1). The blue areas, which do not show any Raman signal associated to graphene- or graphite-like materials (Fig. 2f, ROI-3), are empty holes in a porous structure as revealed by both optical and scanning electron microscopy (SEM).

As shown in Fig. 3a–d, pristine and laser-treated ink-coated wood substrates have dramatically different surfaces. The laser passage generates a highly interconnected porous structure, thanks to a combination of factors which include the intumescent behavior

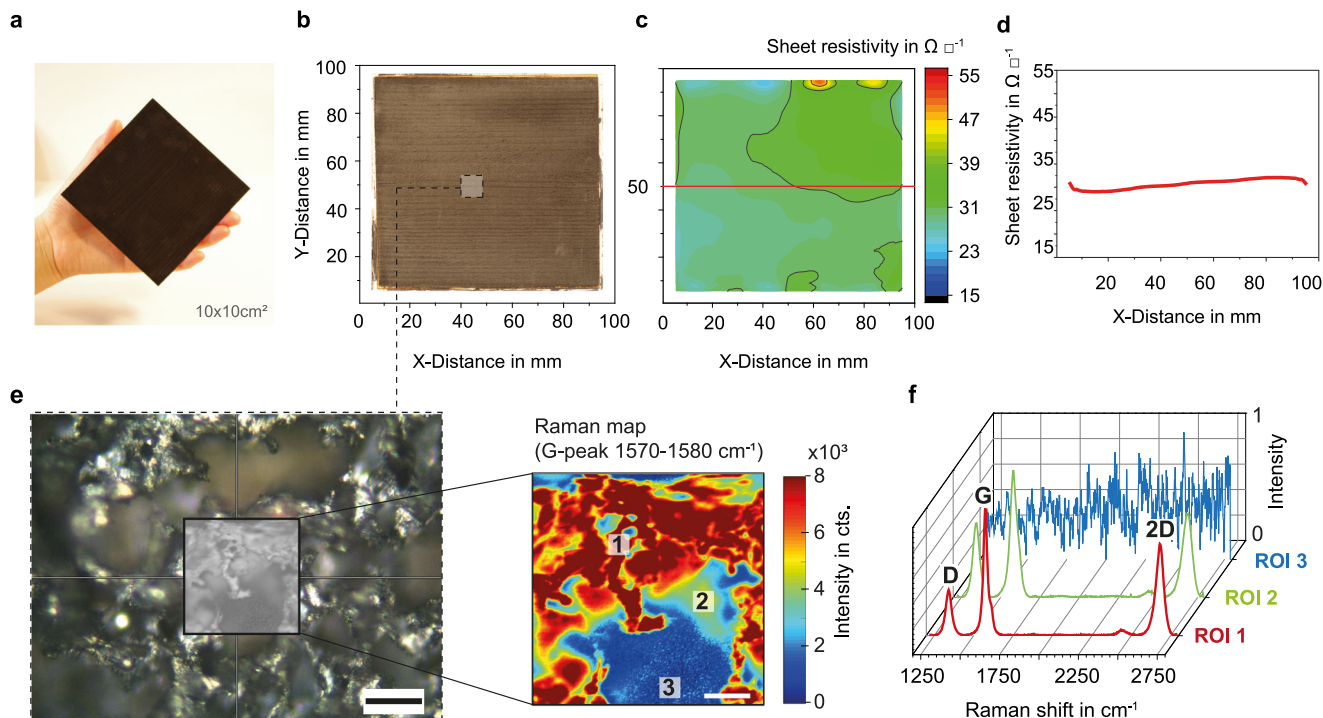


**Fig. 2** Characterization of IC-LIG structures on wood: electrical conductivity and Raman spectroscopy. **a, b** Optical images of a large-scale ( $100\text{ cm}^2$ ) sample of IC-LIG on spruce wood, and **c** its sheet resistivity map (measured with the contactless eddy-current method; see also Supplementary Fig. 4). **d** The horizontal line plot at  $y = 50\text{ mm}$  highlights that the sheet resistivity is constant over a  $10\text{ cm}$  distance. **e** Optical image of the graphitized porous structure and associated Raman map ( $\lambda = 532\text{ nm}$ , scale bar  $50\text{ }\mu\text{m}$ ) of the G-peak ( $1570\text{--}1580\text{ cm}^{-1}$ ). **f** Regions of interest (ROI,  $\sim 15 \times 15\text{ }\mu\text{m}^2$  each) measured at three different positions.

of tannic acid<sup>35</sup>, thermal decomposition processes, and the formation of volatile products<sup>36</sup>. Raman measurements of this structure, performed at different positions (Fig. 3e), revealed that the graphitization process was most successful on the top layer. The pronounced G- ( $\sim 1580\text{ cm}^{-1}$ ) and 2D-peaks ( $2680\text{--}2690\text{ cm}^{-1}$ ), together with a small D-peak ( $\sim 1345\text{ cm}^{-1}$ ), indicated the presence of turbostratic graphene, with partially graphitized carbon domains localized within the first micrometers. Moving toward the wood substrate, the intensity of both G- and 2D-peaks started to decrease. By contrast the D-peak, which is associated to the presence of defects<sup>32,37</sup>, increased, suggesting a higher structural disorder. The degree of graphitization decreased further until the wood substrate was reached, as indicated by an intense background<sup>38</sup>.

These results were in good agreement with those obtained from wide-angle X-ray diffraction (WAXD), where the rotational and translation disorder of  $sp^2$ -hybridized graphene layers suggested this porous microstructure to consist mainly of turbostratic graphene (Supplementary Fig. 5). However, samples treated with high fluence parameters showed emerging (hkl) reflections, indicating partial graphitization<sup>31,36,39,40</sup>. High temperatures during the thermal graphitization of organic materials usually result in both higher degrees of graphitization and bigger crystallites (from  $5$  to  $25\text{ nm}$ )<sup>31</sup>. From the integrated intensity ratio  $I_D/I_G$  (Eq. (1)), we calculated for our nanographite crystals an in-plane crystallite size  $L_a = 22\text{ nm}$ , in good agreement with the value estimated from the (002) reflection in the WAXD diffractogram ( $\approx 25\text{ nm}$ , Eq. (3)) and with literature reports<sup>11,41,31</sup>. By contrast, using a lower laser fluence decreased the quality of the LIG materials produced (Supplementary Figs. 6–9) resulting in carbon products with a less pronounced graphitic structure (lower stacking order) and more disordered (turbostratic) graphene layers with small in-plane crystallite size  $L_a \sim 7\text{ nm}$  (for details, see the Supplementary Information).

A closer structural inspection confirms that the top surface displays the highest degree of graphitization. The morphology of the top surface stands out from the underlying porous carbon (Fig. 3d, g, h). This may be a direct consequence of the different spatio-temporal laser interaction with the surface and bulk of the ink layer. The top surface, being the most exposed to the beam, is expected to absorb the highest amount of energy and consequently to be heated up the most<sup>36</sup>. As shown by energy-dispersive X-ray spectroscopy (EDX), iron is distributed over the entire surface (Fig. 3h). However, its concentration seems to be lower in the areas most exposed to the laser beam (Fig. 3h, Supplementary Table 2). We note here that the volatilization of iron during high-temperature graphitization has been reported before<sup>42</sup>. Observed at higher magnification (Fig. 3d), the porous microstructure appears to be decorated with particles, which transmission electron microscopy (TEM) revealed to be made of a dense iron-rich core surrounded by a lighter carbon foam (Fig. 3i–k)<sup>43,44</sup>. From the WAXD diffractograms, the distribution of iron carbide  $\text{Fe}_3\text{C}$  ( $\theta = 43.9^\circ, 44.6^\circ, 45^\circ$ ) and of iron oxides  $\text{Fe}_x\text{O}_y$  ( $\theta = 43.1^\circ$ )<sup>45,46</sup> within the turbostratic structure could be inferred, but their univocal identification was prevented by the relatively low peak intensities and a diffraction band overlap at  $\theta = 40\text{--}50^\circ$ . The presence of these species is also suggested from X-ray photoelectron spectroscopy (XPS) (Supplementary Fig. 10), more precisely by three signals in the Fe  $2p$  area, respectively at  $710.8$  ( $\text{Fe}^{2+} 2p_{3/2}$ ),  $713.6$  ( $\text{Fe}^{3+} 2p_{3/2}$ ) and  $724\text{ eV}$  ( $\text{Fe}^{2+} 2p_{1/2}$ ) and a peak at  $530\text{ eV}$  (Fe–O) in the O  $1s$  area<sup>47</sup>. In the C  $1s$  plot, a pronounced asymmetric peak at  $284.5\text{ eV}$  ( $sp^2$  carbon) and its  $\pi\text{--}\pi^*$  satellite indicate graphitic carbon<sup>48</sup>. The shift toward higher eV and the peak broadening within the C  $1s$  area is indicative of the presence of iron carbide and oxidized iron species<sup>49,50</sup>, as well as of disordered carbon<sup>48</sup>. The calculated carbon and iron yields for spruce, beech, balsa, oak, and paper samples are summarized in Supplementary Table 2.

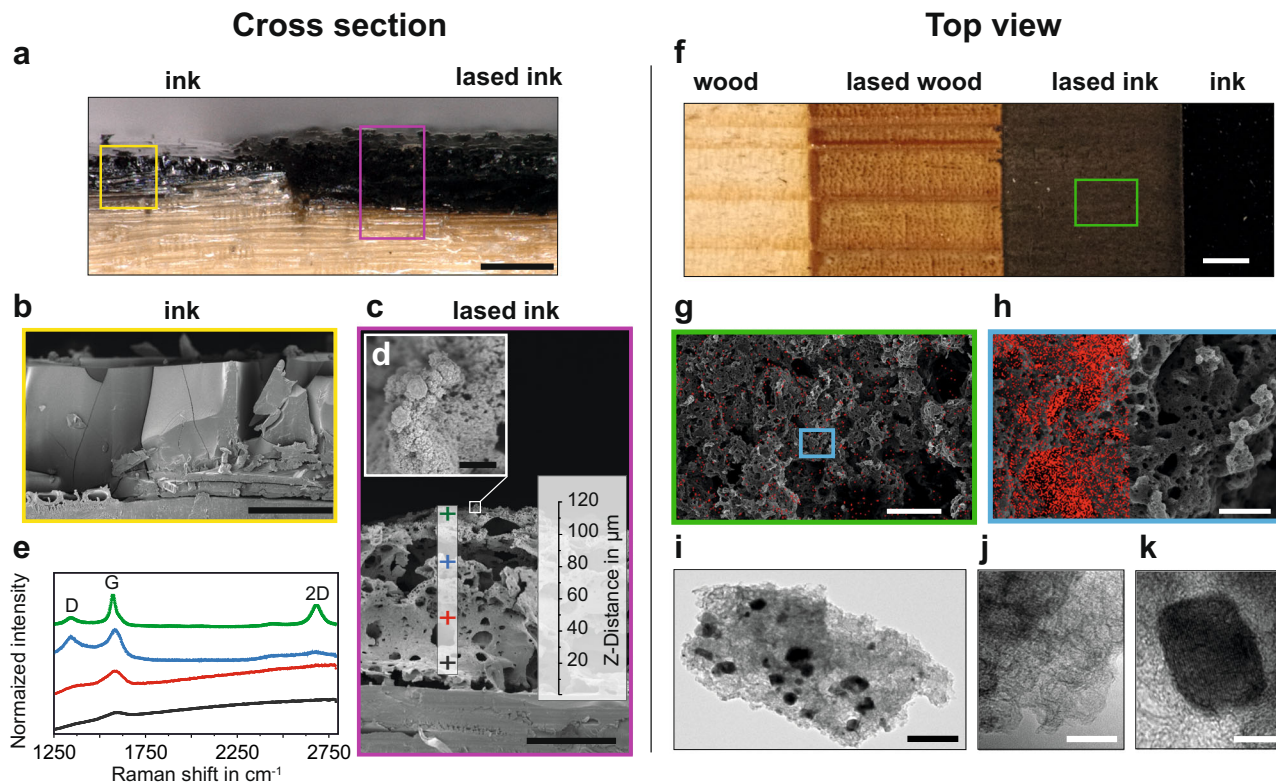


**Fig. 3** Characterization of IC-LIG structures on wood: morphological and structural analysis. **a** Image showing lased and pristine ink-coated spruce veneer from the cross section perspective. SEM images of **(b)** pristine and **(c)** lased ink-coated spruce. The inset **d** is a magnified image of the upper surface showing its nanostructure. In **c**, crosses of different colors indicate the typical Raman measurement points on samples treated with high fluence parameters. The corresponding Raman spectra are shown in **e**. The top view optical image in **f** compares uncoated (left) with ink-coated (right) spruce after laser treatment. **g, h** SEM images (top view) showing the multi-hierarchical porosity of lased ink-coated spruce. **i–k** TEM images of the iron-carbon composite. The dark spots are due to the iron-rich phase. Scale bars: **a** 200  $\mu\text{m}$ , **b** and **c** 50  $\mu\text{m}$ , **d** 1  $\mu\text{m}$ , **f** 10 mm, **g** 100  $\mu\text{m}$ , **h** 25  $\mu\text{m}$ , **i** 20 nm, **j**, **k** 10 nm.

Moreover, both the Raman peaks (Supplementary Fig. 6) and intensity ratios (Supplementary Fig. 7) of the top-surface material showed a striking resemblance with materials obtained by treating organic precursors at very high temperatures, around 2500–3000 °C<sup>11,31,51</sup>. This is remarkable, since such temperature values could hardly be reached by our laser system even with a power up to 13 W. We note here that the bright spark arising from the lasing of ink-coated samples (Supplementary Movie 1, Supplementary Fig. 11) is indicative of the localized generation of high temperatures resulting from ink-laser interactions<sup>41</sup>.

Although beneficial for the graphitization process, the localized generation of high temperatures exceeding the decomposition temperature for cellulose and hemicellulose (above 300 °C) could have a negative influence on wood's mechanical properties<sup>52</sup>. Since converting large-area wood veneers into conductive IC-LIG materials without affecting their mechanical properties is especially important for prospective applications, we performed tensile tests on both native and lased ink-treated spruce and beech veneers. The tensile strength was not reduced as a result of our IC-LIG process (Supplementary Fig. 12).

**Preliminary investigation of IC-LIG mechanism.** It is known that certain transition metal cations, such as iron, can have a beneficial effect on the hydrothermal carbonization and pyrolytic graphitization of organic materials, including wood, thanks to thermo-catalytic effects<sup>13,35,51,53–57</sup>. Since our ink contains iron, it is reasonable to hypothesize that thermo-catalytic processes could have promoted efficient laser-induced graphitization already at temperatures between 1200 °C and 1600 °C, well within the expected reach of our lasing parameters<sup>13,51</sup>. For this reason,

we call our approach iron-catalyzed laser-induced graphitization (IC-LIG).

To better understand the role of iron in IC-LIG, we investigated wood coated with an iron-free ink i.e., containing only tannic acid, gum arabic and glycerol. Fourier-transform infrared (FTIR) measurements indicated that the light absorption in correspondence of our laser emission (1060  $\text{cm}^{-1}$ ) of wood coated with our iron-tannic acid ink is much higher compared to that of native wood and of wood coated with the iron-free ink (Supplementary Fig. 13). For wood substrates coated with the iron-free ink, at least two lasing steps were necessary to develop a measurable electrical conductivity (with sheet resistivity values around 60–70  $\Omega \square^{-1}$ ) with the same laser parameters used to treat iron-tannic acid ink-coated wood. The final product was an irregular carbon foam (Supplementary Fig. 14), devoid of the nano-features observed when using the iron-tannic acid ink. According to the WAXD results, this carbon structure remains completely amorphous even after two laser-engraving steps (Supplementary Fig. 5). Tannic acid is a well-known carbon precursor for high-temperature hydrothermal and pyrolytic carbonization processes<sup>35,58–60</sup>. Our results confirm that this holds for laser-induced graphitization too. They also highlight the crucial role of iron catalysis in promoting its more efficient conversion into high-quality, highly conductive graphite-like materials.

The mechanism for bulk iron-catalyzed thermal graphitization of biomass is already known<sup>13,53,54,57,61–64</sup> and, at least along its general lines, should also apply to our process. Based on this interpretation, the iron-tannic acid complex would be decomposed under the laser first into amorphous carbon and iron oxide

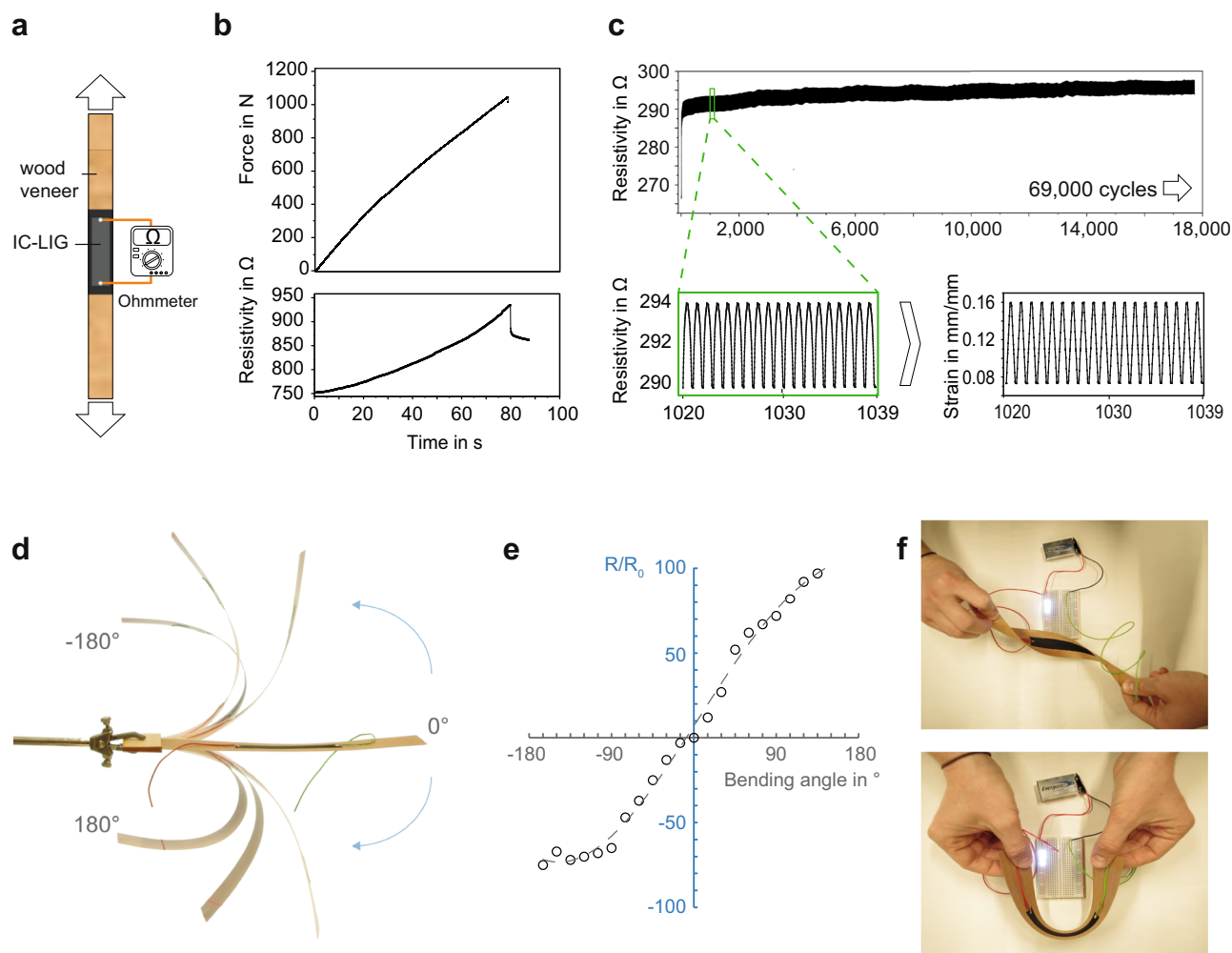


**Fig. 4 IC-LIG-Wood for strain sensors and flexible electrodes.** **a** Schematic representation of a proof-of-concept IC-LIG-wood strain sensor (the arrows indicate the direction of tensile stress application) for measuring the change of resistivity as a function of applied force. **b** Force-time plot with the corresponding resistivity-time plot for a representative IC-LIG-spruce veneer. **c** Resistivity values measured under tensile load cycles with a representative IC-LIG-beech veneer. The measurements were performed for more than 69,000 cycles. The slight increase in resistivity over time is most probably due to the creep of wood veneer during the cycling test. The inset highlights the periodic resistivity change, and the direct correlation between the measured resistivity data from source measure unit with the measured strain values from clip-on extensometer. **d** Picture overlay showing an IC-LIG flexible electrode obtained on a thin cherry wood veneer, which allows for extensive bending angles. **e** Relationship between the bending angle and the associated resistivity change  $R/R_0$ . **f** Pictures showing the stability of electrical connection even under twisting and bending. Here the flexible IC-LIG-wood electrode is used to connect a battery with a LED light.

nanoparticles, followed by conversion into iron carbide  $\text{Fe}_3\text{C}$  by carbothermal reduction. Once the  $\text{Fe}_3\text{C}$  nanoparticles have reached a critical size, the catalyzed graphitization of amorphous carbon could start. We assume that the graphitization processes and the formation of iron oxide nanoparticles would start already in the heat-affected zone, that is, within the focal plane of the laser, where the temperature can reach up to  $350^\circ\text{C}$ <sup>20</sup>. However, because our surface laser treatment is extremely fast compared to more conventional bulk graphitization processes, we expect the growth of  $\text{Fe}_3\text{C}$  particles to be constrained by the time of exposition to high temperatures. Indeed, TEM images show that most of these particles are smaller than 20 nm, and embedded in carbon foam. Thus, the analogy between this mechanism and our process might hold only for the initial moments. Laser-matter interactions most probably play a key role for the iron-catalyzed conversion of amorphous carbon into LIG, and further research is needed to clarify this point. Nevertheless, compared to conventional thermo-catalytic graphitization approaches, our approach requires five times less metal (5.6 wt.% instead of up to 30 wt.%)

and only a single step, making additional substrate impregnation with fire retardants, pre-charring of the precursor at temperatures between  $300\text{--}600^\circ\text{C}$  and heat-treatments under inert atmosphere unnecessary<sup>13,51,65</sup>.

#### Fabrication of IC-LIG-wood electronic devices

**Strain sensor and flexible electrode.** State-of-art structural health monitoring systems are expensive, require dedicated instrumentation, and are difficult to integrate into load-bearing elements without compromising the structural performance of the latter<sup>66</sup>. With the interest for mass timber multi-story buildings on the rise worldwide, it is crucial to provide suitable sensor systems for the assessment of load-bearing wood elements for the improvement of structural design and guarantee serviceability<sup>67</sup>. We show here that, by converting large wood areas into conductive IC-LIG while keeping intact the bulk mechanical properties allows us to reach out for such prospective building-scale applications.

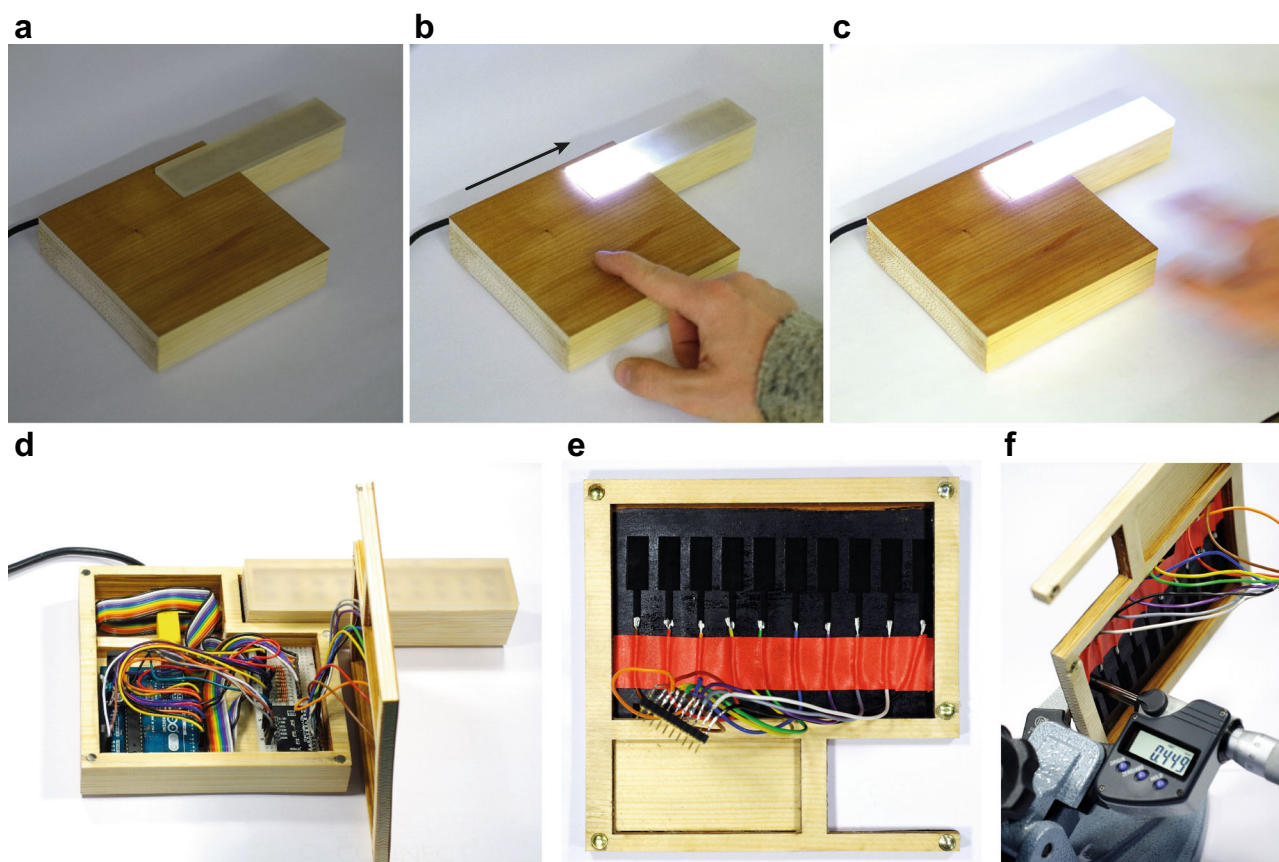


**Fig. 5 IC-LIG-Wood touch button panel.** Capacitive IC-LIG-wood touch button panel made with a thin wild cherry wood veneer. Image sequence showing that the initially “off” (a) LED lights can be switched “on” (b, c) by touching the front native wood veneer surface and moving the finger in the direction indicated by the black arrow. Pictures showing (d) the open device, (e) the rear wood veneer surface with the conductive IC-LIG touch buttons. f Demonstration of how thin the engraved veneer is (maximum thickness 450  $\mu\text{m}$ ).

To make a proof-of-concept strain sensor device we attached electrodes to the conductive IC-LIG area engraved on spruce and beech veneers. We then measured the change in resistivity during a tensile test under constant humidity conditions (Fig. 4a). As shown in Fig. 4b, the mechanical deformation of the wood veneers resulted in a resistivity increase as a function of strain until failure. Cycling tests confirmed that our LIG structures can sustain >69,000 cycles without significant performance losses (Fig. 4c, Supplementary Movie 4).

Inspired by the durability of our IC-LIG-wood strain sensors, we applied the IC-LIG process on thin ( $\sim 450 \mu\text{m}$ ) wild cherry (*Prunus avium* L.) wood veneers to produce highly flexible electrodes (Fig. 4d–f). Even after several fast, irregular flexions at high bending angles, their resistivity always returned to the original value (Supplementary Movie 5). The reason for such robustness is the strong connection between the conductive LIG structures with the underlying wood substrate, resulting in a stability unparalleled compared to that achievable with state-of-art carbon-based inks. We demonstrated this point by subjecting both our IC-LIG-wood electrode and a wood veneer coated with a commercial water-based conductive carbon ink to prolonged (up to 30 min) ultrasonication in water. As shown in Supplementary Fig. 15, our IC-LIG electrode kept its electrical performance even under such harsh conditions, while the carbon-based ink completely separated from the wood substrate. Considering the outstanding performance in terms of flexibility and mechanical strength of our IC-LIG electrodes, we envisage prospective applications as flexible sensors and wearable haptic devices for soft robotics and motion tracking.

*Touch button panel.* Besides structural and flexible sensors, electrically conductive wooden elements could have useful design applications especially as user interfaces. Large wall panels with controls actuated by capacitive sensing could be used e.g., to switch on and off the lights in a smart home. As a proof-of-concept to demonstrate the potential of IC-LIG for real-world, large-scale wood electronics, we built a touch panel with an array of conductive areas or “buttons” that control a dimmable wooden desk lamp, but the same approach could be applied for large wall panels. Thanks to our IC-LIG approach we can make conductive thin veneers from a variety of wood species (Supplementary Fig. 3), selecting the most adequate for the desired application. Wild cherry (*Prunus avium* L.) wood has a high aesthetic value, hence, we chose it to make a touch panel (Fig. 5) by coating one side of a thin ( $\sim 450 \mu\text{m}$ ) wild cherry wood veneer with our iron-tannic acid ink and laser-engraving ten areas or “buttons” (Fig. 5e). We connected each laser-engraved touch button to an Arduino microcontroller equipped with a sensor controller (MPR121 breakout board), while each button was considered to a connected LED. The working principle of this kind of device is self-capacitance, in which an electrode forms a capacitor with the ground plane (earth). Here, each laser-engraved conductive area (touch button) is an electrode, and the ground is the wood veneer itself. By applying a voltage to a button, an electric field is generated. When the native surface on the opposite side of a button is touched, the electric field and consequently the capacitance is changed. The sensor controller detects this touch event and switches on or off the associated LED. Thus, the functionalized cherry wood veneer could be used as a decorative touch panel to

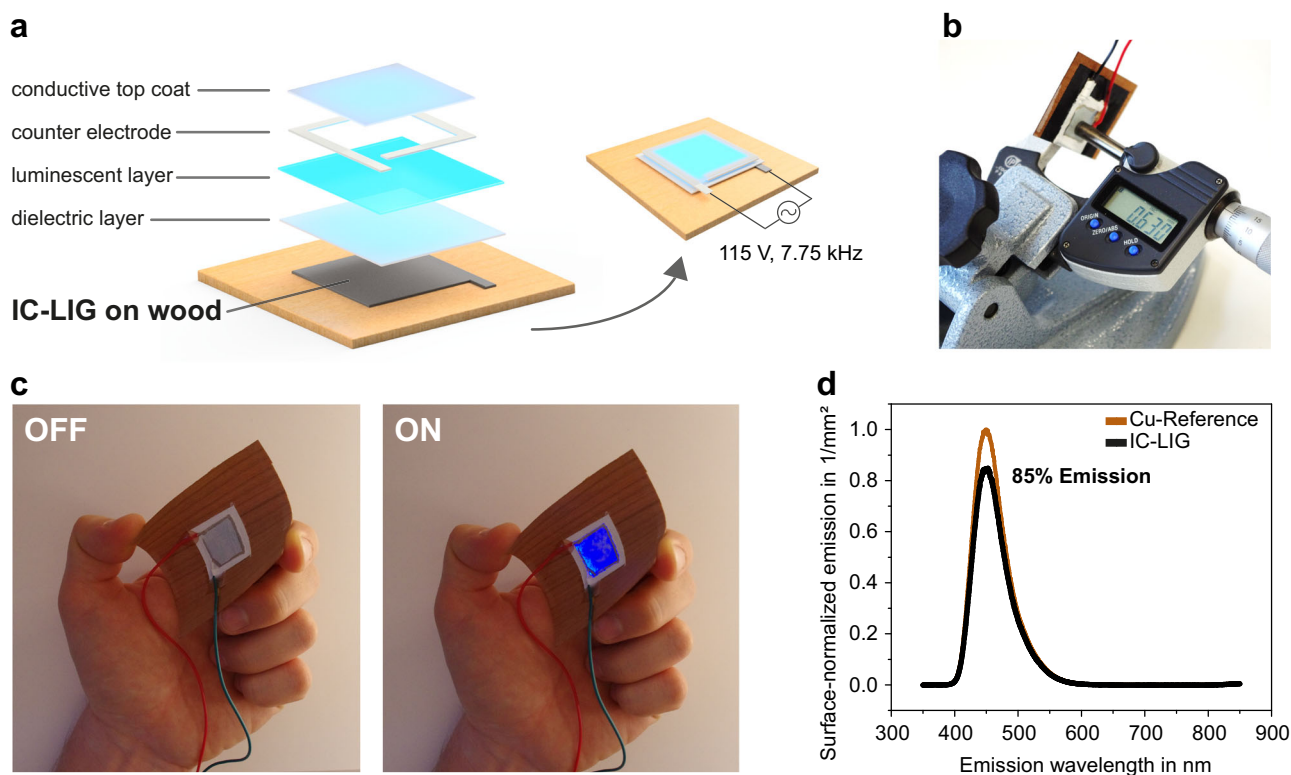


**Fig. 6 IC-LIG-Wood electroluminescent (EL) device.** **a** Exploded view and schematic representation of our IC-LIG-wood EL device. **b** The whole EL device is only 630  $\mu\text{m}$ -thick. **c** Showcasing the operation and flexibility of our IC-LIG-wood EL device. **d** Comparison of light emission efficiency between our EL device, made with an IC-LIG back electrode, and a reference device made with copper-foil as back electrode.

control a dimmable desk lamp (Fig. 5, Supplementary Movies 2 and 3). Each button could also be assigned to a different function, other than switching lights on and off. Such a sustainable smart veneer, combining the esthetic value and unique haptics of wood, could easily find applications as a user interface in the building sector as well as in the automotive industry (e.g., for car dashboards), but also for point-of-sale applications such as vending machines.

**Electroluminescent device.** Electroluminescent (EL) flat panel displays are of growing interest for lighting and optical signaling purposes. However, contemporary research efforts that aim at making EL devices more sustainable are limited to the use of biobased materials (e.g., gelatin<sup>68</sup> and cellulose<sup>69</sup>) as substrates, while the conductive back electrodes remain metal-based (e.g., copper foil, silver paste<sup>68,69</sup>, indium tin oxide ITO<sup>70</sup>). The great environmental benefits of carbon-based electrodes over copper, aluminum and silver electrodes have already been demonstrated for closely-related photovoltaic applications<sup>71</sup>. Here we describe the use of a LIG-based back electrode to fabricate an electroluminescent device, an approach, which has not been reported before. We started by fabricating a  $20 \times 20 \text{ mm}^2$  IC-LIG back electrode on a thin ( $\sim 450 \mu\text{m}$ ) cherry wood veneer. Coating this back electrode first with a standard dielectric paste (barium titanium oxide), then with an electroluminescent phosphor layer (manganese-doped zinc silicate), and eventually with a transparent conductive (PEDOT:PSS) top coating, resulted in a thin ( $\sim 660 \mu\text{m}$ ) flexible EL device (Fig. 6, Supplementary Movie 6). To show the high performance of our IC-LIG back electrode we assembled a control EL device using a standard copper Cu-foil as the back electrode, *ceteris paribus*, and used it for comparison. The luminescent area was comparably homogeneous in both devices (Supplementary Fig. 16), and we proved by direct measurement

that using IC-LIG as back electrode resulted in a light emission efficiency up to 85% compared to that obtained with Cu-foil (Fig. 6d). This is a remarkable achievement, especially taking into account the huge differences between IC-LIG and Cu-foil in terms of electrical conductivity ( $2500 \text{ S m}^{-1}$  vs  $59 \cdot 10^6 \text{ S m}^{-1}$ ) and morphology (porous 3D-structure, resulting in the formation of a slightly thicker dielectric layer, vs flat homogenous surface). Our device emits light already with an operating voltage of 110 V, corresponding to an electric field of  $\sim 1.1 \text{ V } \mu\text{m}^{-1}$ , and a frequency of 7.75 kHz. For comparison, an electric field  $> 5 \text{ V } \mu\text{m}^{-1}$  (with an operating frequency  $> 1 \text{ kHz}$ ) is required to achieve reasonable brightness in conventional flexible EL devices<sup>72</sup>. Furthermore, we observed that by changing the operating voltage and frequency to 325 V and 50 Hz, respectively, the illuminated area became more uniform, and the emitted color changed from blue to light turquoise (Supplementary Fig. 16).

## Discussion

Conventional approaches toward “green” electronics, involving the substitution of plastic substrates with bio-based (e.g., (nano) cellulose) ones, might not be sufficient to tackle the challenges posed by the increasing demand for sustainable electronic products. Inexpensive, abundant and renewable resources must be used not only as substrates but also as conductors, substituting expensive and polluting metals. In this context, conductive carbon materials derived from biological sources could be desirable environmentally friendly alternatives to silver, copper, and aluminum.

Laser-induced graphitization (LIG) is a promising technique for the fabrication of bio-based conductive carbon materials, but conventional processes have great limitations for demanding substrates such as wood and paper, which require multiple lasing



steps in inert atmospheres and the use of hazardous fire retardants, and nevertheless result in high substrate ablation and thermal damage. In this work we addressed and overcame these challenges by applying a new approach, iron-catalyzed laser-induced graphitization (IC-LIG). Using an iron-tannic acid ink and a conventional CO<sub>2</sub> laser, we managed to engrave large ( $\geq 100$  cm<sup>2</sup>) highly conductive (up to 2500 S m<sup>-1</sup>) LIG structures on thin ( $\sim 450$   $\mu$ m) wood veneers (and even on paper) with a single laser step in ambient atmosphere, preserving the substrate mechanical properties and compensating the decreased spatial resolution (due to laser beam defocusing) with an increased processing speed. This favorable fabrication strategy, together with the excellent electrical performance of the obtained products, make our IC-LIG approach especially attractive for prospective industrial-scale applications.

We systematically investigated the interplay between ink, substrate and laser parameters for a variety of wood species, characterizing in detail the properties of the obtained LIG materials with state-of-art techniques. Laser-induced graphitization of iron-tannic acid complexes showed highly beneficial effects on the graphitization of wood and cellulose substrates. Our results pointed out the crucial role of iron promoting the formation of highly conductive LIG, and revealed structure-property relationships for the resulting hierarchically porous graphite-like conductive foam. We mapped large-scale samples with novel eddy-current measurements, demonstrating the homogenous electrical conductivity over the entire sample surface.

To highlight the great potential of IC-LIG for the development of large-scale sustainable wood electronics, we showcased a variety of devices, including a highly durable strain sensor (potentially suitable for structural health monitoring), a flexible electrode, a capacitive touch button panel, and an electroluminescent device. This latter is the first reported example of an electroluminescent device made with LIG as back electrode, which shows a performance comparable to that of a copper-electrode reference. Applications for energy storage devices (e.g., batteries and supercapacitors), requiring porous highly conductive metal-rich structures, are also envisaged for our IC-LIG materials. The high robustness and durability make our IC-LIG materials useful also e.g., in the building and automotive sectors.

## Methods

**Materials.** Tannic acid (source: Chinese natural gall nuts), iron(III) citrate (technical), and glycerol (99+%) were purchased from Sigma-Aldrich. Gum arabic (spray dried) was purchased from Spectrum Chemical. Carbon-based aqueous ink (Bare Conductive<sup>®</sup>, UK) and silver paste (EM-Tec, AG44, Micro to Nano, NL) All chemicals were used as received. Sliced veneers were obtained from Norway spruce (*Picea abies*), beech (*Fagus sylvatica*), oak (*Quercus robur* L.), balsa (*Ochroma pyramidale*), wild cherry (*Prunus avium* L.), and ash (*Fraxinus excelsior*). Rotary cut veneers were obtained from birch (*Betula pubescens*) and maple (*Acer pseudoplatanus* L.). All veneers had a thickness of about 1 mm, unless otherwise stated. Deionized water (DI) was thoroughly used unless otherwise stated.

**Preparation of the iron-tannic acid ink.** Tannic acid (33 g) was dissolved by adding it in small portions under stirring (500 rpm) to 72 g of deionized water pre-heated to 60 °C. With continued heating and stirring, 5 g of gum arabic, 8 g of glycerol, and eventually 7 g of iron(III) citrate were added sequentially in small portions to ensure their complete dissolution. The resulting iron-tannic acid ink was cooled down to room temperature under stirring and stored at room temperature until use.

**Ink deposition on wood and cellulose paper substrates.** The iron-tannic acid ink was applied on thin wood veneers and paper (Whatman) using a commercial paintbrush. Two to three layers of ink were applied to obtain a homogenous coating. The samples were then stored for at least 12 h at 20 °C and 65% RH before use.

**Laser treatment.** Samples were treated with a commercial 10.6  $\mu$ m CO<sub>2</sub> laser engraver (Speedy 300, Trotec). The laser had a maximum power of 60 W and a maximum scan rate of 3.55 m s<sup>-1</sup>. The used parameter for the laser treatment

depended on the substrate. Hence, power ranged between 15 and 30% with scan rates between 150 and 350 mm s<sup>-1</sup>, an image density of 1000 pulses inch<sup>-1</sup>, and a defocus up to 5 mm (resulting beam diameter 0.4 mm). To study the effect of laser fluence on graphitization (Supplementary Figs. 5–9): a laser power of  $\sim 13$  W with an engraving speed of 200 mm s<sup>-1</sup> were the parameters used for high fluence (HiF) samples, while for low fluence (LoF) samples a laser power of  $\sim 12$  W and a scan rate of 270 mm s<sup>-1</sup> were used.

**Characterization techniques.** For electrical properties characterization, squares of size 40  $\times$  40 mm<sup>2</sup> were laser-engraved on 50  $\times$  50 mm<sup>2</sup> wood veneer samples. Sheet resistance was measured using a four-point probe (SD-800, NAGY) and electrical resistivity measurements using a source measure unit (2450, Keithley Instruments, US). Sheet resistance maps were obtained using the EddyCus<sup>®</sup> TF map 2525SR automated sheet resistance mapping device. The samples were mapped with a scanning pitch of 0.25–0.5 mm. The device was calibrated using 50  $\times$  50 mm calibration samples based on NIST reference standards.

Raman spectroscopy was performed with a confocal Raman microscope (Renishaw InVia) using a 532 nm laser, an objective (Zeiss, 20 $\times$ ) and an 1800 l mm<sup>-1</sup> grating. The integral exposure time was 3 s for 10 accumulations covering a spectral range of 1220–2790 cm<sup>-1</sup> with 2 MW laser power for single point measurements. Data of single point measurements of the cross section and top view measurements were evaluated using the software OriginPro 2019 (version 9.6.0.172, OriginLab Corporation, US). For comparing cross section spectra, data were normalized (0,1). For analyzing the FWHM of top view measurements, the peak analysis tool in OriginPro software was used.

As mapping parameters, an integration time of 3 s (single spectrum acquisition) with 2 MW laser power and a step width of 500 nm were used in the Streamline HR mode. After data acquisition, a baseline correction and cosmic ray removal filter were applied using the Wire 3.7 software (Renishaw UK). For chemical imaging, data were exported into CytoSpec (v. 2.00.01), a commercially available MatLab-based software. The integrated intensity of the G-peak band (1575–1585 cm<sup>-1</sup>) was used to obtain a color-scaled representation of the Raman map (200  $\times$  200  $\mu$ m<sup>2</sup>).

Crystallite size  $L_a$  was calculated<sup>11</sup> using Eq. (1), in which the intensity ratio between the D- and G-peaks is inversely proportional to crystallite size:

$$\frac{I_D}{I_G} = \frac{C(\lambda_L)}{L_a} \quad (1)$$

The wavelength-dependent pre-factor  $C$ , for  $L_a$  expected to be  $>2$  nm, following the suggestions of Matthews et al. can be expressed as follows (Eq. (2))<sup>73</sup>:

$$C(\lambda_L) \approx C_0 + \lambda_L C_1 \quad (2)$$

where  $C_0 = -12.6$  nm and  $C_1 = 0.033$ , valid for 400 nm  $< \lambda_L < 700$  nm.

Microstructural measurements were performed using a digital optical microscope (Keyence VHX-6000, Keyence, JP) and open source image analysis software ImageJ (1.53e). Smooth surfaces of cross sections were prepared using a rotary microtome (Leica RM2255, DE). High-resolution micrographs of laser-treated surfaces and cross sections were taken with the in-lens detector of a field-emission scanning electron microscope (SEM, Leo Gemini 1530, Carl Zeiss AG, DE) driven by an accelerating voltage of 2 kV. Energy-dispersive X-ray spectroscopy (UltraDry II, Thermo Fisher Scientific GmbH, DE) driven by a 20 kV acceleration voltage was used to determine the local concentrations of iron and carbon.

Transmission electron microscopy (TEM) imaging was performed with JEM 1400 (JOEL, JP) with an accelerating voltage of 120 kV. Particles were scraped off the samples, suspended in ethanol, deposited on 400 mesh copper grids and subsequently air-dried.

Wide-angle X-ray diffraction (WAXD) was performed with an X-ray diffractometer (Xpert Pro, Panalytical, UK) equipped with a Soller slit and Cu-K $\alpha_1$  radiation source ( $\lambda = 1.540598$  Å) operated at 40 kV and 40 mA. Each scan was done in goni mode with  $2\theta$  angle ranging from 5° to 70° in 0.016° steps. The analysis of crystallite size  $L_a$  was performed for spruce and paper samples by applying the Scherrer equation (Eq. (3)):

$$L_a = \frac{1.84\lambda}{B_{1/2}(2\theta)\cos\theta} \quad (3)$$

where  $B_{1/2}(2\theta)$  (in radian units) is the full width at half maximum of the (101) peak.

The obtained diffraction profiles showed broad peak bands, due to the translational and rotational disorder of the sp<sup>2</sup>-hybridized graphene layers (turbostratic arrangement) resulting in unreliable (hkl) reflections and making them unsuitable for estimating crystallite sizes following the Scherrer equation. Thus, calculating the crystallite sizes with diffraction patterns from samples treated with lower laser fluence was impossible. It is therefore suggested to estimate the crystallite sizes using a fitting approach of scattering profiles developed by Ruland and Smarsly<sup>11,31,36</sup>. However, samples treated with high laser fluence showed more distinct (002) and (101) peaks which allowed a simple estimation using Eq. (3).

X-ray photoelectron spectroscopy (XPS) was performed with a SPECS STM spectrometer (SPECS GmbH, Germany) using a Mg K $\alpha$  X-ray source ( $\lambda = 1253.6$  eV) with a power of 300 W. The measurements were made at room temperature. Each sample was measured at three spots. The investigated area was

typically  $10 \times 7 \text{ mm}^2$ . Survey spectra were acquired over a binding energy range of 0–1000 eV at pass energy of 30 eV and resolution of  $0.5 \text{ eV step}^{-1}$ . High-resolution spectra of C 1s, O 1s and Fe 2p were an average of three scans acquired at a pass energy of 20 eV and resolution of  $0.05 \text{ eV step}^{-1}$ . The spectra were collected in the same order for each sample (survey, C 1s, O 1s, Fe 2p). The CasaXPS software was used for background subtraction (U 2 Tougaard-type), peak integration, quantitative chemical analysis and deconvolution. The C 1s ( $C-C \text{ sp}^2/\text{sp}^3$  overlap) peak at 284.5 eV was used to calibrate the binding energy scale. The C 1s area was deconvoluted in four main signals, 284.5 (C–C, C–H), 285.8 (C–O), 287.3 (C=O), and 289.1 eV (O–C=O) assigned to  $\text{sp}^2$  and  $\text{sp}^3$  carbon, besides a  $\pi-\pi^*$  satellite peak (292.7 eV) and two plasmon loss peaks at 290.8 and 295.3 eV. The survey spectra shows a high amount of carbon for all samples, ranging from 73–83 at.%, which is in good agreement with literature values<sup>36</sup>. The amount of iron is relatively low for both wood (between 1.0 and 2.6 at.%) and paper (~3.3–3.5 at.%) samples, in accordance with EDX results (Supplementary Table 2, Fig. 3h, and Supplementary Fig. 17). The differences observed within the absolute values amongst the samples are possibly related to topographic effects<sup>48</sup>.

Fourier-transform infrared spectroscopy (FTIR) was performed in attenuated total reflection (ATR) mode with a FT-IR spectrometer (Tensor 27, Bruker, Switzerland). The spectra were measured with a resolution of  $1 \text{ cm}^{-1}$  from 4000 to  $400 \text{ cm}^{-1}$  with 32 scans per measurement.

Mechanical tensile tests were performed according to ISO 527-5 with three sample types (Supplementary Fig. 12a): native wood veneer, ink-coated wood veneer, and laser-treated ink-coated wood veneer. Samples were laser-cut from Norway spruce (*Picea abies*) and beech (*Fagus sylvatica*) thin veneers according to standard sample type A ( $250 \times 15 \times 1 \text{ mm}^3$ ). A conductive area of  $20 \times 50 \text{ mm}^2$  centered on the sample surface was laser following our IC-LIG approach. End tabs were glued with commercial polyurethane adhesive. Samples were acclimatized to  $20^\circ\text{C}$  and 65% relative humidity for at least one week. Before testing, electrodes (copper wires) were glued with conductive silver paste to the end of the conductive area and connected to a source measure unit (2450, Keithley Instruments, US) for monitoring the resistivity change during tensile test (Supplementary Fig. 12a). Displacement was measured with a clip-on extensometer and used for a comparison with measured resistivity change. All tests were conducted at a climate condition of  $20^\circ\text{C}$  and 65% relative humidity. An initial load of 5 N was applied thereupon samples were tested with a speed of  $1 \text{ mm min}^{-1}$  until a 50% force drop after the maximal force ( $F_{\text{max}}$ ) had been reached. Cycling test were performed using the same sample measures as we used for tensile tests. Samples were loaded between a nominal strain of 0.5 mm to 1.0 mm with a holding time of 1 s and a speed of  $10 \text{ mm min}^{-1}$ . In parallel, the resistivity change was measured with a source measure unit (2450, Keithley Instruments, US) for monitoring the resistivity change during the cycling test. Due to time constraints, sample was measured for only ~69,000 cycles (69,156 cycles).

**Fabrication of the touch button panel.** To make the touch-sensitive veneer for the dimmable desk lamp demonstrator, we engraved areas or “buttons” (Fig. 5e) on a wild cherry (*Prunus avium* L.) thin veneer (ca.  $450 \mu\text{m}$ ) using our IC-LIG approach. We glued electrodes (copper wires) with conductive silver paste to the end of each touch button to connect them to a capacitive touch sensor breakout (MPR121, SparkFun) and an Arduino microcontroller (Mega 2560). We attached a panel of ten pairs of LEDs to the Arduino via  $220 \Omega$  resistors. Each touch button is connected to a pair of LEDs. The Arduino code is based on Bare Conductive MPR121 Arduino Library<sup>74</sup> and is available upon reasonable request.

**Fabrication and testing of the electroluminescent device.** To make the back electrode, we engraved a  $20 \times 20 \text{ mm}^2$  area on ink-coated cherry wood veneer (~ $450 \mu\text{m}$ ) following our IC-LIG approach. The electroluminescent device was assembled using a commercial kit (LumiLor®, Darkside Scientific, USA). Successive layers were applied on the engraved area, as shown in Fig. 6a, starting with a dielectric (barium titanium oxide), then an electroluminescent phosphor (manganese-doped zinc silicate), and finally a transparent top coating of PEDOT:PSS which, together with conductive silver paste, made the counter electrode. We compared the efficiency of our IC-LIG-wood electroluminescent device with that of a reference device, made using copper foil as the back electrode, by measuring the electroluminescence (EL) spectra with an Agilent Cary Eclipse spectrofluorimeter. To ensure accurate measurements all samples were placed in the same position, as close as possible to the detector. The bio/chemiluminescence mode of the spectrofluorimeter was set, collecting spectra from 350 to 850 nm, with a resolution of 0.5 nm and the emission slit set to 2.5.

## Data availability

The data that support the findings of this study can be found in the article and the Supplementary Information files. Any other relevant data are available from the corresponding author upon request.

Received: 27 May 2022; Accepted: 13 June 2022;

Published online: 27 June 2022

## References

- Irimia-Vladu, M. “Green” electronics: biodegradable and biocompatible materials and devices for sustainable future. *Chem. Soc. Rev.* **43**, 588–610 (2014).
- Bol, D., de Streeel, G. & Flandre, D. Can we connect trillions of IoT sensors in a sustainable way? A technology/circuit perspective (Invited). In: *2015 IEEE SOI-3D-Subthreshold Microelectronics Technology Unified Conference (S3S)*, <https://doi.org/10.1109/S3S.2015.7333500> (2015).
- Pan, K. et al. Sustainable production of highly conductive multilayer graphene ink for wireless connectivity and IoT applications. *Nat. Commun.* **9**, 5197 (2018).
- Keplinger, T., Wang, X. & Burgert, I. Nanofibrillated cellulose composites and wood derived scaffolds for functional materials. *J. Mater. Chem. A* **7**, 2981–2992 (2019).
- De France, K., Zeng, Z., Wu, T. & Nystrom, G. Functional materials from nanocellulose: utilizing structure-property relationships in bottom-up fabrication. *Adv. Mater.* **33**, e2000657 (2021).
- Aeby, X., Poulin, A., Siqueira, G., Hausmann, M. K. & Nystrom, G. Fully 3D Printed and Disposable Paper Supercapacitors. *Adv. Mater.* **33**, e2101328 (2021).
- Guo, H. et al. Dictating anisotropic electric conductivity of a transparent copper nanowire coating by the surface structure of wood. *J. R. Soc. Interface* **15**, <https://doi.org/10.1098/rsif.2017.0864> (2018).
- Fu, Q., Chen, Y. & Sorieul, M. Wood-Based Flexible Electronics. *ACS Nano* **14**, 3528–3538 (2020).
- Wan, J. et al. Highly anisotropic conductors. *Adv. Mater.* **29**, <https://doi.org/10.1002/adma.201703331> (2017).
- Byrne, C. E. & Nagle, D. C. Carbonization of wood for. *Adv. Mater. Appl. Carbon* **35**, 7 (1997).
- Zickler, G. A., Smarsly, B., Gierlinger, N., Peterlik, H. & Paris, O. A reconsideration of the relationship between the crystallite size  $L_a$  of carbons determined by X-ray diffraction and Raman spectroscopy. *Carbon* **44**, 3239–3246 (2006).
- Kwon, J. H., Park, S. B., Ayrlimis, N., Oh, S. W. & Kim, N. H. Effect of carbonization temperature on electrical resistivity and physical properties of wood and wood-based composites. *Compos. Part B Eng.* **46**, 102–107 (2013).
- Ramirez-Rico, J., Gutierrez-Pardo, A., Martinez-Fernandez, J., Popov, V. V. & Orlova, T. S. Thermal conductivity of Fe graphitized wood derived carbon. *Mater. Des.* **99**, 528–534 (2016).
- Kurra, N., Jiang, Q., Nayak, P. & Alshareef, H. N. Laser-derived graphene: a three-dimensional printed graphene electrode and its emerging applications. *Nano Today* **24**, 81–102 (2019).
- Ye, R., James, D. K. & Tour, J. M. Laser-induced graphene: from discovery to translation. *Adv. Mater.* **31**, e1803621 (2019).
- Ye, R. et al. Laser-induced graphene formation on wood. *Adv. Mater.* **29**, <https://doi.org/10.1002/adma.201702211> (2017).
- Chyan, Y. et al. Laser-induced graphene by multiple lasing: toward electronics on cloth, paper, and food. *ACS Nano* **12**, 2176–2183 (2018).
- Edberg, J. et al. Laser-induced graphitization of a forest-based ink for use in flexible and printed electronics. *npj Flexible Electr.* **4**, <https://doi.org/10.1038/s41528-020-0080-2> (2020).
- Dallinger, A., Keller, K., Fitzek, H. & Greco, F. Stretchable and skin-conformable conductors based on polyurethane/laser-induced graphene. *ACS Appl Mater. Interfaces* **12**, 19855–19865 (2020).
- Le, T. S. D., Park, S., An, J., Lee, P. S. & Kim, Y. J. Ultrafast laser pulses enable one-step graphene patterning on woods and leaves for green electronics. *Adv. Funct. Mater.* **29**, <https://doi.org/10.1002/adfm.201902771> (2019).
- Niemz, P., Sonderegger, W. & Hering, S. Thermal conductivity of Norway spruce and European beech in the anatomical directions. *Forestry Wood Technol.* **72**, 66–72 (2010).
- Lee, H. et al. Iron gall ink revisited: in situ oxidation of Fe(II)-tannin complex for fluidic-interface engineering. *Adv. Mater.* **30**, e1805091 (2018).
- Rahim, M. A. et al. Coordination-driven multistep assembly of metal–polyphenol films and capsules. *Chem. Mater.* **26**, 1645–1653 (2014).
- Ponce, A. et al. Elucidation of the Fe(III) gallate structure in historical iron gall ink. *Anal. Chem.* **88**, 5152–5158 (2016).
- Canevari, C. et al. Chemical characterization of wood samples colored with iron inks: insights into the ancient techniques of wood coloring. *Wood Sci. Technol.* **50**, 1057–1070 (2016).
- Yang, S. et al. The interaction of phenolic acids with Fe(III) in the presence of citrate as studied by isothermal titration calorimetry. *Food Chem.* **157**, 302–309 (2014).
- Nam, S. et al. A reinforced thermal barrier coat of a Na–tannic acid complex from the view of thermal kinetics. *RSC Adv.* **9**, 10914–10926 (2019).
- Perron, N. R. & Brumaghim, J. L. A review of the antioxidant mechanisms of polyphenol compounds related to iron binding. *Cell Biochem. Biophys.* **53**, 75–100 (2009).
- Kolar, J. et al. Historical iron gall ink containing documents — properties affecting their condition. *Analytica Chim. Acta* **555**, 167–174 (2006).

30. Ferrari, A. C. & Basko, D. M. Raman spectroscopy as a versatile tool for studying the properties of graphene. *Nat. Nanotechnol.* **8**, 235–246 (2013).
31. Schuepfer, D. B. et al. Assessing the structural properties of graphitic and non-graphitic carbons by Raman spectroscopy. *Carbon* **161**, 359–372 (2020).
32. Barros, E. B. et al. Raman spectroscopy of graphitic foams. *Phys. Rev. B* **71**, <https://doi.org/10.1103/PhysRevB.71.165422> (2005).
33. Ferrari, A. C. Raman spectroscopy of graphene and graphite: disorder, electron-phonon coupling, doping and nonadiabatic effects. *Solid State Commun.* **143**, 47–57 (2007).
34. Barros, E. B., Souza Filho, A. G., Son, H. & Dresselhaus, M. S. G' band Raman lineshape analysis in graphitic foams. *Vibrational Spectrosc.* **45**, 122–127 (2007).
35. Deng, Y. et al. Highly effective and stable doped carbon catalyst with three-dimensional porous structure and well-covered Fe<sub>3</sub>C nanoparticles prepared with C<sub>3</sub>N<sub>4</sub> and tannic acid as template/precursors. *J. Power Sources* **417**, 117–124 (2019).
36. Wang, H. et al. Laser-carbonization: Peering into the formation of micro-thermally produced (N-doped) carbons. *Carbon* **176**, 500–510 (2021).
37. Casiraghi, C. Probing disorder and charged impurities in graphene by Raman spectroscopy. *Phys. Status Solidi Rapid Res. Lett.* **3**, 175–177 (2009).
38. Gierlinger, N., Keplinger, T. & Harrington, M. Imaging of plant cell walls by confocal Raman microscopy. *Nat. Protoc.* **7**, 1694–1708 (2012).
39. Li, Z. Q., Lu, C. J., Xia, Z. P., Zhou, Y. & Luo, Z. X-ray diffraction patterns of graphite and turbostratic carbon. *Carbon* **45**, 1686–1695 (2007).
40. Hishiyama, Y. & Nakamura, M. X-ray diffraction in oriented carbon films with turbostratic structure. *Carbon* **33**, 1399–1403 (1995).
41. Lin, J. et al. Laser-induced porous graphene films from commercial polymers. *Nat. Commun.* **5**, 5714 (2014).
42. Andrews, R., Jackques, D., Qian, D. & Dickey, E. C. Purification and structural annealing of multiwalled carbon nanotubes at graphitization temperatures. *Carbon* **39**, 1681–1687 (2001).
43. Gerber, O. et al. Design of Fe<sub>3</sub>-xO<sub>4</sub> raspberry decorated graphene nanocomposites with high performances in lithium-ion battery. *J. Energy Chem.* **25**, 272–277 (2016).
44. Ding, X. et al. Sustainable solid-state strategy to hierarchical core-shell structured Fe<sub>3</sub>O<sub>4</sub>@graphene towards a safer and green sodium ion full battery. *Electrochim. Acta* **260**, 882–889 (2018).
45. Braghioroli, F. et al. Hydrothermal treatment of tannin: a route to porous metal oxides and metal/carbon hybrid materials. *Inorganics* **5**, <https://doi.org/10.3390/inorganics5010007> (2017).
46. Yu, Z. L. et al. Ion-catalyzed synthesis of microporous hard carbon embedded with expanded nanographite for enhanced lithium/sodium storage. *J. Am. Chem. Soc.* **138**, 14915–14922 (2016).
47. Wu, Z. Y. et al. Iron carbide nanoparticles encapsulated in mesoporous Fe-N-doped carbon nanofibers for efficient electrocatalysis. *Angew. Chem. Int. Ed. Engl.* **54**, 8179–8183 (2015).
48. Blume, R. et al. Characterizing graphitic carbon with X-ray photoelectron spectroscopy: a step-by-step approach. *ChemCatChem* **7**, 2871–2881 (2015).
49. Diekmann, G. Pa. W. The bonding state of carbon segregated to  $\alpha$ -iron surfaces and on iron carbide surfaces studied by electron spectroscopy. *Surf. Sci.* **160**, 253–270 (1985).
50. Kaspar, P. et al. Characterization of Fe<sub>2</sub>O<sub>3</sub> thin film on highly oriented pyrolytic graphite by AFM, Ellipsometry and XPS. *Appl. Surf. Sci.* **493**, 673–678 (2019).
51. Sagues, W. J. et al. A simple method for producing bio-based anode materials for lithium-ion batteries. *Green. Chem.* **22**, 7093–7108 (2020).
52. Bekhata, P. & Niemz, P. Effect of high temperature on the change in color, dimensional stability and mechanical properties of spruce wood. *Holzforchung* **57**, 539–546 (2003).
53. Hoekstra, J. et al. Base metal catalyzed graphitization of cellulose: a combined raman spectroscopy, temperature-dependent X-ray diffraction and high-resolution transmission electron microscopy study. *J. Phys. Chem. C* **119**, 10653–10661 (2015).
54. Glatzel, S., Schnepf, Z. & Giordano, C. From paper to structured carbon electrodes by inkjet printing. *Angew. Chem. Int. Ed. Engl.* **52**, 2355–2358 (2013).
55. Bonnet, F. et al. Study of the oxide/carbide transition on iron surfaces during catalytic coke formation. *Surf. Interface Anal.* **34**, 418–422 (2002).
56. Hunter, R. D. et al. The effect of precursor structure on porous carbons produced by iron-catalyzed graphitization of biomass. *Mater. Adv.* **1**, 3281–3291 (2020).
57. Hoekstra, J. et al. The effect of iron catalyzed graphitization on the textural properties of carbonized cellulose: magnetically separable graphitic carbon bodies for catalysis and remediation. *Carbon* **107**, 248–260 (2016).
58. Jurkiewicz, K. et al. Conversion of natural tannin to hydrothermal and graphene-like carbons studied by wide-angle X-ray scattering. *J. Phys. Chem. A* **119**, 8692–8701 (2015).
59. Tondi, G., Fierro, V., Pizzi, A. & Celzard, A. Tannin-based carbon foams. *Carbon* **47**, 1480–1492 (2009).
60. Titirici, M. M. et al. Sustainable carbon materials. *Chem. Soc. Rev.* **44**, 250–290 (2015).
61. Thompson, E., Danks, A. E., Bourgeois, L. & Schnepf, Z. Iron-catalyzed graphitization of biomass. *Green. Chem.* **17**, 551–556 (2015).
62. Yan, Q. et al. Catalytic graphitization of kraft lignin to graphene-based structures with four different transitional metals. *J. Nanoparticle Res.* **20**, <https://doi.org/10.1007/s11051-018-4317-0> (2018).
63. Lotz, K. et al. Tuning the properties of iron-doped porous graphitic carbon synthesized by hydrothermal carbonization of cellulose and subsequent pyrolysis. *ACS Omega* **4**, 4448–4460 (2019).
64. Gutiérrez-Pardo, A., Ramírez-Rico, J., Cabezas-Rodríguez, R. & Martínez-Fernández, J. Effect of catalytic graphitization on the electrochemical behavior of wood derived carbons for use in supercapacitors. *J. Power Sources* **278**, 18–26 (2015).
65. Banek, N. A., Abele, D. T., McKenzie, K. R. & Wagner, M. J. Sustainable conversion of lignocellulose to high-purity, highly crystalline flake potato graphite. *ACS Sustain. Chem. Eng.* **6**, 13199–13207 (2018).
66. Palma, P. & Steiger, R. Structural health monitoring of timber structures – review of available methods and case studies. *Constr. Build. Mater.* **248**, <https://doi.org/10.1016/j.conbuildmat.2020.118528> (2020).
67. Jockwer, R., Grönquist, P. & Frangi, A. Long-term deformation behaviour of timber columns: monitoring of a tall timber building in Switzerland. *Eng. Struct.* **234**, <https://doi.org/10.1016/j.engstruct.2021.111855> (2021).
68. Zhang, X. et al. Sustainable and transparent fish gelatin films for flexible electroluminescent devices. *ACS Nano* **14**, 3876–3884 (2020).
69. Tsuneyasu, S. et al. Enhancement of luminance in powder electroluminescent devices by substrates of smooth and transparent cellulose nanofiber films. *Nanomaterials* **11**, <https://doi.org/10.3390/nano11030697> (2021).
70. Ji, J. et al. Three-phase electric power driven electroluminescent devices. *Nat. Commun.* **12**, 54 (2021).
71. Espinosa, N., Laurent, A., dos Reis Benatto, G. A., Hösel, M. & Krebs, F. C. Which electrode materials to select for more environmentally friendly organic photovoltaics? *Adv. Eng. Mater.* **18**, 490–495 (2016).
72. Yin, H., Zhu, Y., Youssef, K., Yu, Z. & Pei, Q. Structures and materials in stretchable electroluminescent devices. *Adv. Mater.*, e2106184, <https://doi.org/10.1002/adma.202106184> (2021).
73. Matthews, M. J., Pimenta, M. A., Dresselhaus, G., Dresselhaus, M. S. & Endo, M. Origin of dispersive effects of the Raman D band in carbon materials. *Phys. Rev. B*, **59**, R6585 (1999).
74. Conductive, B. *Bare conductive MPR121 Arduino library*, <https://github.com/BareConductive/mpr121#readme> (2020).

## Acknowledgements

Yong Ding received funding in the framework of the SNF Project “Hierarchical cellulose scaffolds for structural and functional gradient materials” (200021\_184821/1). Thomas Schneider (ETH Zürich) is gratefully acknowledged for cutting wood samples. Marek Chrapa and Dr. Yaroslav Romanuk (Laboratory for Thin Films and Photovoltaics, Empa) are acknowledged for their help in preliminary electrical resistivity measurements. Dr. Arndt Remhof (Empa) is acknowledged for technical support for XRD. The authors gratefully acknowledge ScopeM for technical support for electron microscopy.

## Author contributions

C.H.D., H.G., I.B. and G.P. conceived the study. C.H.D., H.G. and G.P. designed the experiments. C.H.D. performed the experiments, acquired data, assembled and tested the devices. M.R. contributed to the realization of the IC-LIG-wood electroluminescent device. Y.D. acquired the TEM images. R.G. acquired XPS data. E.P. acquired EDX data. T.K. contributed advice on Raman spectroscopy. C.H.D. and G.P. prepared the manuscript. G.P. and I.B. supervised the project. All authors commented on the manuscript.

## Competing interests

The authors declare no competing interests.

## Additional information

**Supplementary information** The online version contains supplementary material available at <https://doi.org/10.1038/s41467-022-31283-7>.

**Correspondence** and requests for materials should be addressed to Ingo Burgert or Guido Panzarasa.

**Peer review information** *Nature Communications* thanks the anonymous reviewers for their contribution to the peer review of this work.

**Reprints and permission information** is available at <http://www.nature.com/reprints>

**Publisher's note** Springer Nature remains neutral with regard to jurisdictional claims in published maps and institutional affiliations.



**Open Access** This article is licensed under a Creative Commons Attribution 4.0 International License, which permits use, sharing, adaptation, distribution and reproduction in any medium or format, as long as you give appropriate credit to the original author(s) and the source, provide a link to the Creative Commons license, and indicate if changes were made. The images or other third party material in this article are included in the article's Creative Commons license, unless indicated otherwise in a credit line to the material. If material is not included in the article's Creative Commons license and your intended use is not permitted by statutory regulation or exceeds the permitted use, you will need to obtain permission directly from the copyright holder. To view a copy of this license, visit <http://creativecommons.org/licenses/by/4.0/>.

© The Author(s) 2022